Frontiers of Optoelectronics (2025) 18:15
https://doi.org/10.1007/s12200-025-00159-1

Frontiers of Optoelectronics

RESEARCH ARTICLE

Unveiling local molecular desorption dynamics using higher-order optical resonances

Mingquan Deng[1] · Xiujie Dou[1] · Xiaoyu Wang[2] · Yin Yin[3] · Xun Guan[4] · Libo Ma[5] · Xing Ma[1] · Jiawei Wang[1]

Received: 10 March 2025 / Accepted: 9 July 2025
© The Author(s) 2025

Abstract
Understanding the sorption dynamics between water molecules and various solid surfaces is of great interest in diverse fundamental and industrial research. For studying such dynamics in a microsystem, existing investigations mainly focus on sorption behaviors mediated by external temperature variations. Here, we demonstrate a route to in situ sensitive detection of laser irradiation-induced localized water molecule desorption at a sub-monolayer level on an oxide surface. Harnessing a tailored set of optical whispering-gallery-mode (WGM) resonances in a nanomembrane-based microtube cavity, the desorption can be tracked by resonance mode shift in real-time, and further explained using a combination of pseudo-first-order and pseudo-second-order models. Additionally, upon adjusted laser excitation locations, the axial-mode-dependent responses enable the retrieval of corresponding profiles of desorption-induced perturbation at equilibrium. This study provides new insights into molecular desorption kinetics and introduces a spatially resolved sensing technique with applications in surface science, molecular sensing, and the study of desorption dynamics at the nanoscale.

Keywords Microtube cavity · Whispering-gallery-mode (WGM) · Molecular desorption · High-order axial mode · Optical sensing

1 Introduction

Understanding the interactions between water molecules and solid surfaces, such as sorption, diffusion, and permeation, essentially forms the foundation of various fundamental and applied research areas, such as surface and interface physics [1–4], biophysics [5], and catalysis [6, 7]. Nowadays, various label-free optical sensing technologies, leveraging interference or resonance phenomena, have been extensively investigated for high-sensitivity detection of target molecules in both aqueous [8–11] and air environments [12, 13]. A large variety of optical approaches have proven effective for measuring bulk water content (e.g., refractive index sensing) [14, 15] and humidity [16–18]. In contrast to bulk sensing, when significantly fewer water molecules interact with sensors, one should consider molecular properties and morphologies rather than macroscopic refractivity. Typically, the characterization of water molecules on solid surfaces at the sub-monolayer level was conducted using scanning tunneling microscopy (STM) [19], and low-energy electron diffraction (LEED) [20], whereas the demonstration using optical sensors remains elusive.

Among the developed label-free optical sensing platforms, whispering-gallery-mode (WGM) microcavities have garnered significant interest due to their ability of tight optical confinement strong light-analyte interaction, offering detection limits down to the single-molecule level (e.g., DNAs [21, 22], viruses [23], and proteins [10, 24]). The versatility of WGM-based optical sensors has been

✉ Xiaoyu Wang
xiaoyuwang@hainanu.edu.cn

✉ Xing Ma
maxing@hit.edu.cn

✉ Jiawei Wang
wangjw7@hit.edu.cn

1 School of Integrated Circuits, Harbin Institute of Technology (Shenzhen), Shenzhen 518055, China

2 School of Physics and Optoelectronic Engineering, Hainan University, Haikou 570228, China

3 School of Materials Science and Engineering, Jiangsu University, Zhenjiang 212013, China

4 Tsinghua Shenzhen International Graduate School, Tsinghua University, Shenzhen 518055, China

5 Leibniz IFW Dresden, Dresden 01069, Germany

Published online: 28 July 2025

demonstrated across a range of microcavity geometries, including microspheres [12, 15, 25, 26], microdisks [27, 28], microrings [29–31], microtoroids [18, 32–34], and microtubes [13, 14, 35–38]. Among these, microtubular-shaped WGM, particularly those fabricated via nanomembrane origami techniques, stand out due to their hollow-core architecture with sub-wavelength-thick cavity walls, offering superior surface sensitivity to molecular adsorption and desorption [39]. Besides, the flexibility of fabricating nanomembrane-based WGM sensors from diverse materials (e.g., oxides and semiconductors) makes them ideal for probing fine interactions between various non-conductive surfaces and small molecules such as water [37, 38, 40], ethanol [15, 38], and volatile organic compounds (VOCs) [12]. In our prior work [38, 41], the dynamics of water molecular adsorption and release on the oxide surface, as well as the corresponding morphologies of water nanostructures, have been revealed using WGM resonances in nanomembrane-based WGM sensors. However, these investigations primarily relied on external thermal control (e.g., leveraging a liquid helium cryostat [36]), leaving the influence of light irradiation (e.g., via a tightly-focused laser beam) on these interactions largely underexplored.

In this work, the laser-triggered interaction between water molecules and oxide surfaces is unveiled using sculptured three-dimensional (3D) resonances in a rolled-up microtube formed with a tailored nanomembrane design. By continuously monitoring the mode blueshift in the WGM resonant photoluminescence (PL) spectrum, we achieve in situ tracking of the laser-triggered desorption of water molecules at the hydrophobic oxide surface with sub-monolayer level. Compared with conventional WGMs mostly confined into a plane, here tracking of 3D higher-order axial resonance modes enables spatially resolved molecular sensing in real-time, which reflects the profile of perturbation from local laser irradiation. Our proposed approach provides new insights into molecular dynamics at the water/solid interface, offering a powerful tool for studying water-related phenomena and the impact of local light irradiation on molecular processes.

2 Results

2.1 Working principle

Figure 1a and b illustrates the detection process of water molecule desorption, utilizing WGM resonant light emission from a rolled-up nanomembrane microtube cavity. The microtube is fabricated via a well-established nano-origami rolling technique [42], which allows precise control over key structural parameters, including tube size, wall thickness, and winding number. The primary advantage of the technique lies in its ability to engineer resonance profiles along the axial dimension via tailoring the 2D planar nanomembrane geometry into an extruded "lobe" design [43–46]. The presence of the lobe effectively forms an optical quasi-potential well, splitting the original WGM resonance into multiple higher-order axial modes [47–50]. In contrast to the widely-studied microbottle resonators supporting 3D axial resonances [47], the microtube resonators empowered by nanomembrane origami technique feature ultra-thin cavity wall thickness down to several tens of nanometers. Consequently, strong evanescent fields of the set of distinct axial modes are supported at the cavity surface, facilitating the detection of water molecule sorption dynamics [38, 40]. By incorporating defects or gain materials [37] into the dielectric nanomembrane, WGM emission can be excited via optical pumping using a focused laser beam. Given the localized heating due to focused pumping (with a spot size of ~ 1 μm^2), higher-order axial modes exhibit distinct responses due to the varying spatial overlap between the resonant fields and the perturbed area due to laser irradiation (see Fig. 1b). By analyzing the responses of the mode set measured simultaneously and applying perturbation theory [51], the associated desorption profile can be determined.

In experiments, silicon nitride (SiN_x) microtubes are fabricated using our latest dry-release-based nanomembrane origami technique (see Fig. 1c). The center portion of the 2D nanomembrane was tailored into a parabolic-like shape upon lithography and etching (see Methods, Sect. 5). Due to the amorphous nature of the deposited SiN_x nanomembrane film [42, 52, 53], defects-induced broadband PL between 600 and 800 nm gets excited and coupled into WGMs while optically pumped with a 532 nm laser. The measured resonant spectrum in Fig. 1d reveals distinct axial mode families for each mode group defined with different azimuthal mode number M, ranging from the fundamental mode (with axial mode number $l = 0$) to the fourth higher-order mode ($l = 4$). Given the subwavelength thickness of the microtube wall (~ 250 nm), only transverse-magnetic (TM) polarized WGM resonances (with the electric field oriented parallel to the microtube axis) are well-supported [15]. To further investigate the spatial distribution of these higher-order axial modes, spatially resolved measurements were performed (see Methods, Sect. 5). In Fig. 1d, the difference in mode antinode numbers clearly corresponds to the axial mode order. Based on numerically solving the quasi-Schrödinger equation for the lobe-induced optical quasi-potential well, theoretical calculations in Fig. 1f show excellent agreement with the measured mode field distributions (see Fig. 1e).

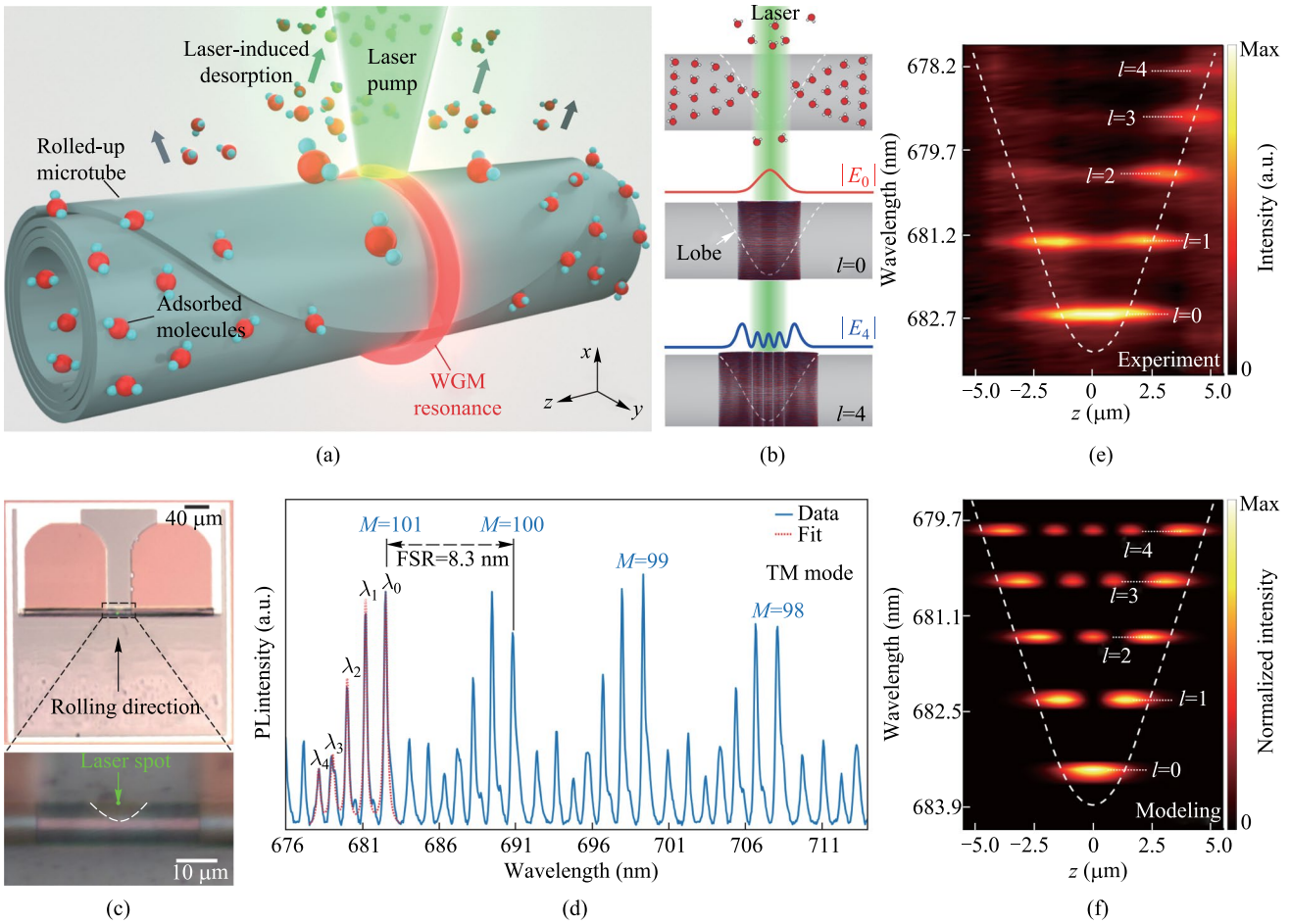

Fig. 1 **a** Schematic illustration of probing laser irradiation-induced water molecule desorption via monitoring the mode shift. **b** Schematics showing the localized laser heating and triggered molecular desorption along the axial axis (top), and the corresponding distribution of the fundamental axial mode (middle, $l=0$) and the fourth-order axial mode (bottom, $l=4$). The curves denote the electric field intensity distributions. **c** Bright-field optical microscope images of the microtube cavity under 10×(top) and 50×(bottom) magnification, with the white dashed line outlining the lobe structure. **d** Measured resonant spectrum (in the range of $M=98-101$) showing higher-order axial modes. The resonant wavelengths of discernable axial modes ($M=101$) are denoted as $\lambda_0-\lambda_4$, respectively. **e** Experimentally measured spatial distribution of axial modes ($l=0-4$). **f** Numerically modeled spatial distribution of axial modes ($l=0-4$). The white dashed lines indicate the optical quasi-potential well

2.2 In situ characterizations of water desorption

In the sensing experiment, the group of axial modes around 677.5 − 683.5 nm with the same azimuthal mode number $M=101$ is tracked (see Fig. 2a), enabling the resonant wavelengths to serve as in situ probes for molecular desorption-induced perturbations. Initially, the laser intensity is set to a low value using a neutral density (ND) filter (optical density = 1) (see $t=-80$ s to 0 s in Fig. 2b), and the resonant wavelength of the fundamental mode remains highly stable in thermal equilibrium with negligible heating effects under low laser excitation power. In Fig. 2a, this behavior is consistent across all axial modes. At $t=0$ s, the laser power was increased tenfold. One can clearly discern a continuous blueshift of the resonant modes, which is attributed to the laser irradiation-induced desorption of water molecules from the microtube surface. Given the nature of weak perturbation, the magnitude of the mode shift $\Delta\lambda$ can be expressed using perturbation theory [38, 41, 51] based on the following formula:

$$\frac{\Delta\lambda}{\lambda}\approx\frac{\Delta\omega}{\omega}=-\frac{\left\langle E(\vec{r})\left|\Delta\varepsilon(\vec{r})\right|E(\vec{r})\right\rangle}{2\left\langle E(\vec{r})\left|\varepsilon(\vec{r})\right|E(\vec{r})\right\rangle},\tag{1}$$

where λ, ω, $E(\vec{r})$, and $\varepsilon(\vec{r})$ are the resonance wavelength, resonance angular frequency, the electric field distribution in the resonator, and the permittivity, respectively. Here $\Delta\varepsilon(\vec{r})$

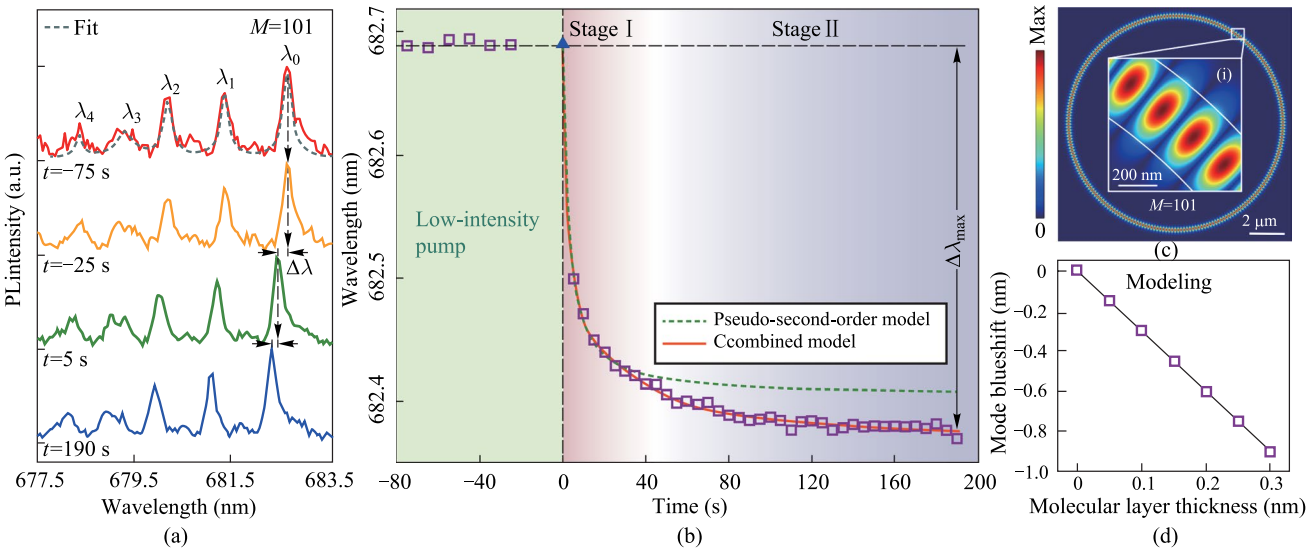

Fig. 2 **a** Temporal evolution of resonance spectra under varying laser excitation intensities at the center of the lobe ($z=0$ μm). Gray line: multi-peak Lorentzian fit to extract the resonant wavelengths for each axial mode. **b** Summarized temporal variation of the resonant wavelength for the fundamental mode. Lines: fits based on the pseudo-second-order model (green, $k_2=-1.30$ s^{-1}) and the combined model (orange, $k_2=-1.30$ s^{-1}, $k_1=-4.55$ s^{-1}). **c** Simulated mode field intensity distribution of the cross-section of a microtube cavity. Inset: Zoomed-in view. **d** Mode shift as a function of the equivalent released molecular layer thickness derived using perturbation theory

denotes the permittivity variation induced by the change of absorbates.

According to the calculation of the perturbation theory, $\Delta\lambda/\lambda$ is linearly proportional to the amount of desorbed water molecules proportion $\Delta q/q$ (or effectively the molecular layer thickness assuming a uniform coverage). In Fig. 2b, for the fundamental mode, the blueshift saturates at ~ −0.31 nm by $t=190$ s under continuous laser-induced heating. Figure 2c presents the simulated mode field distribution at $M=101$ through finite element method. Numerical calculations in Fig. 2d indicate that this shift corresponds to the desorption of a ~ 0.1-nm-thick water layer (corresponding to 33% of a monolayer). The limited strength of desorption is attributed to the hydrophobic nature of the Al_2O_3 surface. Considering the spectral resolution of ~ 20 pm, the estimated noise-equivalent detection limit can be down to ~ 2% change of a water monolayer.

To further analyze the desorption dynamics, we apply the statistical rate theory (SRT) as a widely adopted approach to describe the kinetic behavior of adsorbates (e.g., water molecules) on the solid surface in a gas/solid or solution/solid system [54–57]. The desorption rate is expressed in its general form as [56]:

$$\frac{\mathrm{d}q(t)}{\mathrm{d}t}=K_{ls}c_e\left(1-\frac{q_e}{q_m}\right)\left[K_Lc\left(\frac{q_m-q(t)}{q(t)}\right)^{1/\nu}-\frac{1}{K_Lc}\left(\frac{q(t)}{q_m-q(t)}\right)^{1/\nu}\right], \tag{2}$$

where $q(t)$ is the amount of adsorbates on the solid surface at time t, q_e is the amount at final equilibrium, q_m is the monolayer capacity, K_{ls} is the reaction rate constant, and K_L is the system equilibrium constant. Here c denotes the concentration, c_e is the concentration at the equilibrium, and ν is the heterogeneity parameter ranging from 0 to 1 (with $\nu=1$ corresponding to the ideally homogeneous surface).

Given the complexity, the SRT model is often simplified into the pseudo-first-order and pseudo-second-order models [58, 59]. In Fig. 2b, for $t=0-30$ s, we define the period exhibiting a rapid and intense mode blueshift as "Stage I". The fast response is attributed to the primary desorption, which can be well fitted via a single pseudo-second-order kinetic model:

$$\frac{\Delta q(t)}{q_0}=\frac{q(t)-q_0}{q_0}=\frac{q_e-q_0}{q_0}-\frac{1}{k_2t+q_0/(q_e-q_0)}=\frac{\Delta q_{\max}}{q_0}-\frac{1}{k_2t+q_0/\Delta q_{\max}}, \tag{3}$$

where $\Delta q(t)$ is the amount of desorbed molecules at time t, q_0 is the initial amount of adsorbates, $\Delta q_{\max}$ is the accumulated amount at final equilibrium, and k_2 is the desorption time scale factor, which depends on the initial concentration and the system temperature. The fit in Fig. 2b yields $k_2=-1.30$ s^{-1}, $\Delta q_{\max}/q_0$ of −0.29. Notably, for $t>30$ s, the tracked mode shift gradually deviates from the prediction using the pseudo-second-order model, suggesting the potential contribution of an additional mechanism. In

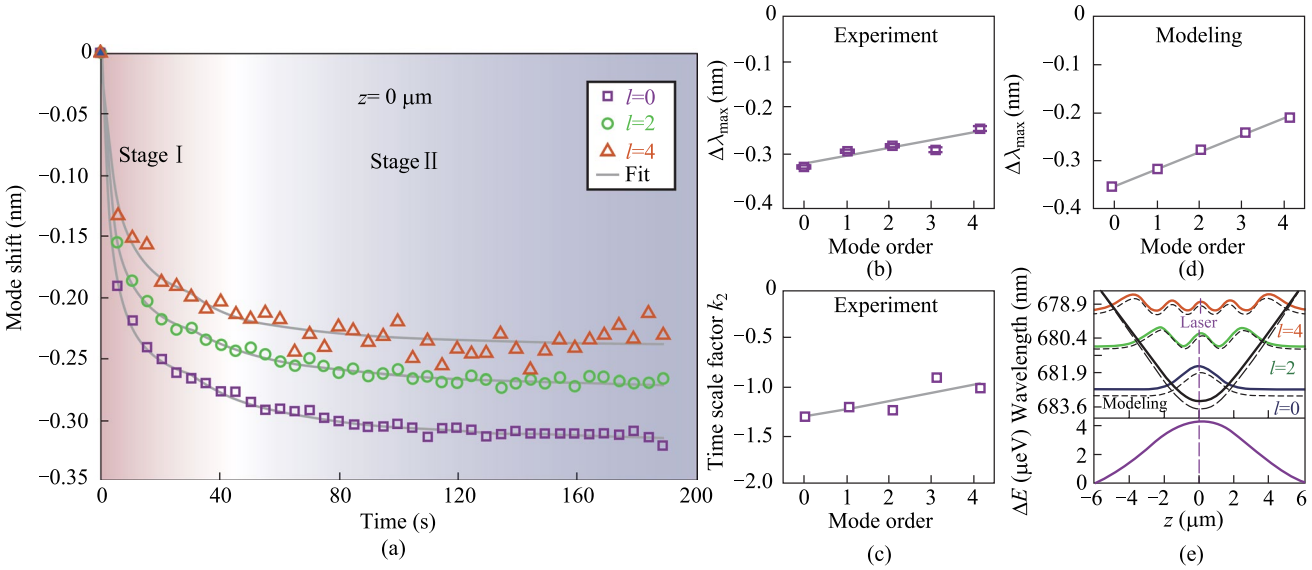

Fig. 3 **a** Summarized temporal variation of the resonance wavelength shifts for three axial modes ($l=0$, 2, and 4) under high laser intensity focused at the center of the lobe ($z=0$ μm). **b** Summarized $\Delta\lambda_{max}$ as a function of the axial mode order. **c** Summarized time scale factor k_2 as a function of the axial mode order. **d** Numerically calculated $\Delta\lambda_{max}$ using perturbation theory. The gray lines in **b** and **d** serve as visual guides. **e** Top: Numerically calculated spatial distribution of axial modes ($l=0$, 2, and 4) at the original state (dashed lines) and final equilibrium (solid lines) due to laser radiation. The black lines denote the boundary of the optical quasi-potential wells at the original state (dashed line) and final equilibrium (solid line). Bottom: corresponding laser irradiation-induced perturbation on the potential well. The purple dotted line denotes the location of laser irradiation

previous studies, the pseudo-first-order kinetic model has been employed for the prediction of molecular dynamics near equilibrium [56]. Here for $t=30-190$ s, we define the period exhibiting a smooth and moderate mode blueshift as "Stage II". Due to its distinct behavior compared to Stage I, we propose a combined model incorporating contributions from both pseudo-first-order and pseudo-second-order dynamics:

$$\frac{\Delta q(t)}{q_0} = w_1\left(\frac{\Delta q_{max}}{q_0} - \frac{\Delta q_{max}}{q_0}e^{-k_1 t}\right) + w_2\left(\frac{\Delta q_{max}}{q_0} - \frac{1}{k_2 t + q_0/\Delta q_{max}}\right), \quad (4)$$

where k_1 is the desorption time scale factor of the pseudo-first-order dynamics, and w_1 and w_2 are the weighting factors of two mechanisms. The fit for Stage II in Fig. 2b suggests a dominant contribution from the pseudo-second-order dynamics with $w_2=2.46$, with a minor contribution from the pseudo-first-order dynamics ($w_1=0.73$).

2.3 Laser irradiation-induced desorption resolved by axial resonances

Given the laser irradiation is predominantly localized to the micrometer scale, the mode-dependent response is studied by tracking the mode shift of all discernable axial modes with the same M (101 as an example). Initially, the laser spot is aligned at the lobe center ($z=0$ μm). As illustrated in Fig. 3a, the tracked mode shift for three axial modes with $l=0$, 2 and 4 reveal distinct desorption rates and saturation levels while reaching the equilibrium. As summarized in Fig. 3b, the lower-order modes, more concentrated around the center of the lobe (see Fig. 1e), experience a stronger perturbation, and consequently a larger mode blueshift. Meanwhile, the mode shift at the initial stage is analyzed by fitting using Eq. (3). The fundamental mode features the lowest value of k_2 of -1.30 s^{-1}, indicating the fastest molecular desorption. In contrast, higher-order axial modes exhibit slightly prolonged desorption processes.

At the final equilibrium ($t\sim190$ s), the mode-dependent responses can be interpreted as spatially-resolved in situ detection of molecular dynamics. By modeling the laser-induced desorption as a Gaussian distribution along the axial direction, we find that the desorbed water molecules induce a global modification of the optical quasi-potential well. Setting the lateral dimension of the irradiation-induced

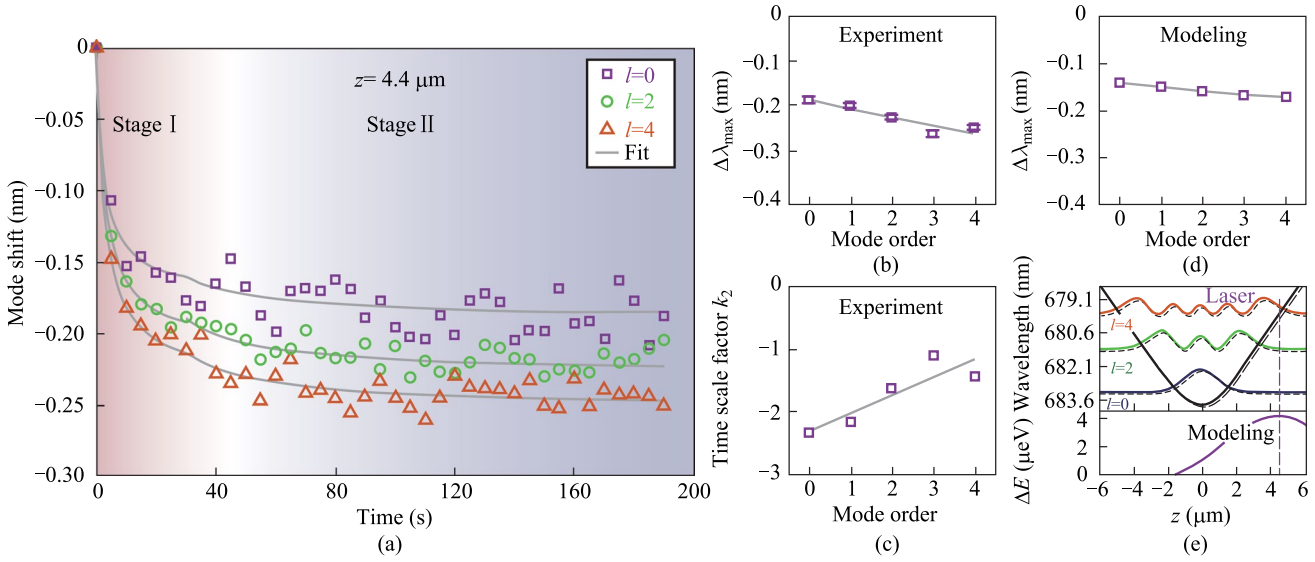

Fig. 4 **a** Summarized temporal variation of the resonance wavelength shifts for three axial modes ($l=0$, 2, and 4) under high laser intensity with the focus shifted away from the center of the lobe ($z=4.4$ μm). **b** Summarized $\Delta\lambda_{max}$ as a function of the axial mode order. **c** Summarized time scale factor k_2 as a function of the axial mode order. **d** Numerically calculated $\Delta\lambda_{max}$ using perturbation theory. The gray lines in **b** and **d** serve as visual guides. **e** Top: Numerically calculated spatial distribution of axial modes ($l=0$, 2, and 4) at the original state (dashed lines) and final equilibrium (solid lines) due to laser radiation. The black lines denote the boundary of the optical quasi-potential wells at the original state (dashed line) and final equilibrium (solid line). Bottom: corresponding laser irradiation-induced perturbation on the potential well. The purple dotted line denotes the displaced position of laser irradiation

perturbation $\Delta\lambda$ to ~ -0.31 nm, one can numerically calculate the perturbed axial modes, including resonant wavelengths and the spatial mode field distributions (see Fig. 3d). The trend of extracted $\Delta\lambda_{max}$ in the calculation is consistent with the experimental observations in Fig. 3b.

To further investigate the axial mode-dependent responses during molecular desorption, additional experiments were conducted with the laser spot displaced from the lobe center to $z=4.4$ μm, while maintaining the same experimental configuration. As shown in Fig. 4a, all three discernable modes exhibit mode blueshift similar to those observed in Fig. 3a. Here the signal–noise ratio, particularly for the fundamental mode, becomes degraded, due to the weakened signals collected by the objective lens at the shifted axial position. The corresponding mode shift for the fundamental mode is less pronounced, decreasing significantly to -0.19 nm compared to -0.31 nm in Fig. 3a. In contrast, the higher-order axial mode $l=4$ suggests the largest mode shift, reaching up to -0.25 nm. This result highlights the strongest spatial overlap between the laser focus and the mode field intensity maximum for $l=4$, which occurs at approximately 4.4 μm, as predicted by the calculated mode field distributions in Fig. 1e.

Consistent with the finding of the time scale factor k_2 in Fig. 3, here, the fundamental mode again suggests the fastest response with k_2 of -2.34 s^{-1}. For higher-order modes, the enhanced disparity k_2 between each mode may arise from the difference in local irradiation strength, which gradually decays from the right side ($z>0$) across the center to the left side ($z<0$), while the spatial inhomogeneity results in distinct rates of reaching local dynamic equilibrium. In numerical calculations, by adopting a shifted location to $z=4.4$ μm for setting the irradiation-induced perturbation, the quasi-potential well gets deformed as a whole. Furthermore, the resulting $\Delta\lambda_{max}$ for all axial modes shows a nice agreement with the observation in Fig. 4b.

3 Conclusion

In summary, we have experimentally demonstrated the detection of surface molecular dynamics using tailored 3D WGM resonances in a nanomembrane-based tubular cavity. Unlike previous studies that primarily focused on molecular adsorption/desorption processes over large variations of the environmental temperature, here our in situ characterization of mode shifts from WGM emission reveals the dynamics of laser irradiation-triggered, local desorption of water molecules from oxide surfaces, achieving a resolution at sub-monolayer level. The axial-mode-dependent responses, together with theoretical analysis based on perturbation theory, elucidate the profile of localized perturbation upon the varying irradiation location and corresponding perturbed optical quasi-potential well. This work provides new insights into the thermal desorption kinetics of water molecules and their spatially resolved interactions on hydrophobic oxide

thin films. Besides, it is envisaged that the technology can be further applied to various types of irradiation-mediated molecular dynamics such as photodegradation, biological transformation, and protein–protein interactions, offering implications for both fundamental studies and practical applications in surface science and molecular sensing.

4 Methods

4.1 Device fabrication

The devices were fabricated using a dry-etching-based nanomembrane origami technique, as described in our previous work [42]. The composite nanomembrane, consisting of an Al_2O_3 stop layer, a Si sacrificial layer, an Al_2O_3 protection layer, a SiN_x strained layer, and another Al_2O_3 protection layer was prepared on a silicon wafer via chemical vapor deposition (for SiN_x and Si) and atomic layer deposition (for Al_2O_3). A photoresist layer (AZ-5214E, Microchemicals GmbH, Germany) was spin-coated onto the nanomembrane and patterned using a maskless lithography (MLA 100, Heidelberg Instruments Mikrotechnik GmbH). Reactive ion etching (RIE, Plasma Laboratory 100; Oxford Instruments PLC, Abingdon, UK) was used to etch the patterned trenches into the sacrificial layer. The entire sample was then passivated with an Al_2O_3 thin film. After opening a release window to define the starting rolling edge, the strained nanomembrane self-assembled into microtubular structures through strain relaxation in a xenon difluoride etching system (Xactix e2 Orbotech Ltd., Yavne, Israel), followed by an additional Al_2O_3 passivation layer. By adjusting the stress condition of SiN_x layer, the diameter of the microtube could be well controlled within the range of ~ 10 – 20 μm. A U-shaped design was employed to ensure a gap between the center of the microtube and the substrate, effectively reducing the loss of microcavity WGM leakage to the substrate, achieving a quality factor (Q) of ~ 2000.

4.2 Optical characterizations

Resonant spectra of the microtube cavities were collected using a confocal photoluminescence setup (LabRAM HR Evolution, HORIBA Scientific) following the same procedure in our previous study [15]. The laser spot displacement was adjusted using a motorized stage, which translated the microtube cavity under focused irradiation. A 532 nm continuous-wave laser (Cobolt Samba) was employed to generate a focused spot with a diameter of ~ 1 μm^2 through a long-distance working objective (Olympus LMPLFLN 50 ×; numerical aperture = 0.5). The laser intensity was adjusted using a neutral density filter wheel. PL signals were collected using the same objective lens, and measured using a spectrometer equipped with a 600 blz/mm grating and an electrically cooled charge-coupled device (CCD) camera. The spatial distributions of axial modes were mapped by translating the microtube cavities from – 6 to 6 μm with a step of 0.1 μm along the z-axis through a motorized stage.

4.3 Sensing tests

The chip containing integrated microtube cavities was mounted in a custom-designed chamber with a volume of ~ 0.7 cm^3. The chamber was constructed with a substrate, a spacer, and a 0.17-mm-thick cover glass and sealed by ultraviolet-curing optical adhesives (NOA 68). A saturated K_2SO_4 solution was prepared and slowly delivered to the chamber using a syringe, offering a constant relative humidity of ~ 60% RH at room temperature (25 °C). The temporal resolution of the current spectral acquisition system is ~ 1 ms, enabling the tracking of fast transient processes. During the studies of laser-induced molecular desorption, the resonant spectra were repeatedly measured with a time resolution of 5 s, ensuring a high signal-to-noise ratio through sufficient integration time.

Acknowledgements The authors acknowledge the support from the National Key R&D Program of China under Grant 2023YFE0208700, the National Natural Science Foundation of China under Grants 62422503, 12474375, 12274182, and 62305093, Science and Technology Innovation Commission of Shenzhen under Grants JCYJ20220531095604009, JCYJ20240813104819027, RCYX20221008092907027, and GXWD20231129101105001, Hainan Province "Nanhai New Star" Science and Technology Innovation Talent Platform Program under Grant NHXXRCXM202304, and the Innovation/Entrepreneurship Program of Jiangsu Province under Grants JSSCTD202146 and JSSCRC2021538.

Authors contributions JWW, XM, and XYW conceived the study. MQD, and XJD performed the theoretical calculations and analysis. XYW, and YY fabricated the samples. MQD, XJD, and XM conducted the optical characterizations and sensing measurements. MQD and XJD analyzed the data. MQD, XJD, LBM, and JWW wrote the manuscript. All authors discussed the results and contributed to the manuscript.

Availability of data and materials The data that support the findings of this study are available from the corresponding authors, upon reasonable request.

Declarations

Competing interests The authors declare that there are no competing interests.

Open Access This article is licensed under a Creative Commons Attribution 4.0 International License, which permits use, sharing, adaptation, distribution and reproduction in any medium or format, as long as you give appropriate credit to the original author(s) and the source, provide a link to the Creative Commons licence, and indicate if changes were made. The images or other third party material in this article are included in the article's Creative Commons licence, unless indicated otherwise in a credit line to the material. If material is not

included in the article's Creative Commons licence and your intended use is not permitted by statutory regulation or exceeds the permitted use, you will need to obtain permission directly from the copyright holder. To view a copy of this licence, visit http://creativecommons.org/licenses/by/4.0/.

References

1. Carrasco, J., Hodgson, A., Michaelides, A.: A molecular perspective of water at metal interfaces. Nat. Mater. **11**(8), 667–674 (2012)
2. Chen, L., Huang, S., Ras, R.H.A., Tian, X.: Omniphobic liquid-like surfaces. Nat. Rev. Chem. **7**(2), 123–137 (2023)
3. Ruiz-Lopez, M.F., Francisco, J.S., Martins-Costa, M.T.C., Anglada, J.M.: Molecular reactions at aqueous interfaces. Nat. Rev. Chem. **4**(9), 459–475 (2020)
4. Groß, A., Sakong, S.: Ab initio simulations of water/metal interfaces. Chem. Rev. **122**(12), 10746–10776 (2022)
5. Dargaville, B.L., Hutmacher, D.W.: Water as the often neglected medium at the interface between materials and biology. Nat. Commun. **13**(1), 4222 (2022)
6. Huang, S., Xu, Y., Zhou, T., Xie, M., Ma, Y., Liu, Q., Jing, L., Xu, H., Li, H.: Constructing magnetic catalysts with in-situ solid-liquid interfacial photo-fenton-like reaction over Ag_3PO_4@$NiFe_2O_4$ composites. Appl. Catal. B Environ **225**, 40–50 (2018)
7. Zhou, B., Gao, R., Zou, J.J., Yang, H.: Surface design strategy of catalysts for water electrolysis. Small **18**(27), 2202336 (2022)
8. Gohring, J.T., Dale, P.S., Fan, X.: Detection of HER2 breast cancer biomarker using the opto-fluidic ring resonator biosensor. Sens. Actuators B: Chem. **146**(1), 226–230 (2010)
9. Dantham, V.R., Holler, S., Barbre, C., Keng, D., Kolchenko, V., Arnold, S.: Label-free detection of single protein using a nanoplasmonic-photonic hybrid microcavity. Nano Lett. **13**(7), 3347–3351 (2013)
10. Guo, Z., Qin, Y., Chen, P., Hu, J., Zhou, Y., Zhao, X., Liu, Z., Fei, Y., Jiang, X., Wu, X.: Hyperboloid-drum microdisk laser biosensors for ultrasensitive detection of human IgG. Small **16**(26), 2000239 (2020)
11. Wang, Z., Fang, G., Gao, Z., Liao, Y., Gong, C., Kim, M., Chang, G.E., Feng, S., Xu, T., Liu, T., Chen, Y.C.: Autonomous microlasers for profiling extracellular vesicles from cancer spheroids. Nano Lett. **23**(7), 2502–2510 (2023)
12. Qiagedeer, A., Yamagishi, H., Hayashi, S., Yamamoto, Y.: Polymer optical microcavity sensor for volatile organic compounds with distinct selectivity toward aromatic hydrocarbons. ACS Omega **6**(32), 21066–21070 (2021)
13. Yang, S., Wang, Y.Q., Kong, Y., Huang, G.S., Zhao, Z., Wang, Y., Xu, B.R., Cui, J.Z., Mei, Y.F.: Enhanced evanescent field coupling of smart particles in tubular optical microcavity for sensing application. Adv. Opt. Mater. **10**(4), 2102158 (2022)
14. Madani, A., Harazim, S.M., Quiñones, V.A.B., Kleinert, M., Finn, A., Naz, E.S.G., Ma, L.B., Schmidt, O.G.: Optical microtube cavities monolithically integrated on photonic chips for optofluidic sensing. Opt. Lett. **42**(3), 486–489 (2017)
15. Wang, J.W., Li, J., Sun, S.Q., Dong, H.Y., Wu, L., Zhao, E.G., He, F., Ma, X., Zhao, Y.S.: Revealing molecular diffusion dynamics in polymer microspheres by optical resonances. Sci. Adv. **9**(19), eadf1725 (2023)
16. Ma, Q.L., Huang, L., Guo, Z.X., Rossmann, T.: Spectral shift response of optical whispering-gallery modes due to water vapor adsorption and desorption. Meas. Sci. Technol. **21**(11), 115206 (2010)
17. Hou, L.T., Li, Y., Fu, Y.M., Yang, J.R., Xu, W.J., Song, X.K., Li, J.J., Liu, Y., Ran, L.L.: Ultra-sensitive optical fiber humidity sensor via Au-film-assisted polyvinyl alcohol micro-cavity and Vernier effect. IEEE Trans. Instrum. Meas. **71**, 1–9 (2022)
18. Mehrabani, S., Kwong, P., Gupta, M., Armani, A.M.: Hybrid microcavity humidity sensor. Appl. Phys. Lett. **102**(24), 241101 (2013)
19. Guo, J., Meng, X., Chen, J., Peng, J., Sheng, J., Li, X.Z., Xu, L., Shi, J.R., Wang, E., Jiang, Y.: Real-space imaging of interfacial water with submolecular resolution. Nat. Mater. **13**(2), 184–189 (2014)
20. Hodgson, A., Haq, S.: Water adsorption and the wetting of metal surfaces. Surf. Sci. Rep. **64**(9), 381–451 (2009)
21. Wan, H., Zhang, S., Gu, Y., Xiong, J., Xu, J., Wan, C., Chao, J.: Label-free, ultra-low detection limit DNA biosensor using high quality optical microcavity functionalized by DNA tetrahedral nanostructure probes. Nanophotonics **12**(16), 3323–3331 (2023)
22. Wang, Z., Liu, Y., Wang, H., Wang, S., Liu, K., Xu, T., Jiang, J., Chen, Y.C., Liu, T.: Ultra-sensitive dnazyme-based optofluidic biosensor with liquid crystal-Au nanoparticle hybrid amplification for molecular detection. Sens. Actuators B: Chem. **359**, 131608 (2022)
23. Dantham, V.R., Holler, S., Kolchenko, V., Wan, Z., Arnold, S.: Taking whispering gallery-mode single virus detection and sizing to the limit. Appl. Phys. Lett. **101**(4), 043704 (2012)
24. Ozgur, E., Roberts, K.E., Ozgur, E.O., Gin, A.N., Bankhead, J.R., Wang, Z., Su, J.: Ultrasensitive detection of human chorionic gonadotropin using frequency locked microtoroid optical resonators. Anal. Chem. **91**(18), 11872–11878 (2019)
25. Zhan, Y.X., Hou, F.Y., Feng, S.F., Wang, X.K., Sun, W.F., Ye, J.S., Zhang, Y.: The distribution and evolution of refractive index in a polystyrene whispering gallery microcavity during glass transition. Adv. Opt. Mater. **10**(17), 2102548 (2022)
26. Capocefalo, A., Gentilini, S., Barolo, L., Baiocco, P., Conti, C., Ghofraniha, N.: Biosensing with free space whispering gallery mode microlasers. Photon. Res. **11**(5), 732–741 (2023)
27. Mao, W.B., Li, F., Jia, D., Zhang, Q., Yang, L.: On-chip multimode WGM microresonator with cross-correlation algorithm for enhanced sensing. Laser Photonics Rev. **18**(8), 2301303 (2024)
28. Gavartin, E., Verlot, P., Kippenberg, T.J.: A hybrid on-chip optomechanical transducer for ultrasensitive force measurements. Nat. Nanotechnol. **7**(8), 509–514 (2012)
29. Hodaei, H., Hassan, A.U., Wittek, S., Garcia-Gracia, H., El-Ganainy, R., Christodoulides, D.N., Khajavikhan, M.: Enhanced sensitivity at higher-order exceptional points. Nature **548**(7666), 187–191 (2017)
30. Guo, R., He, Q., Zhang, Z., Xu, Y., Zhang, S., Lang, Q., Xiao, S., Han, P., Wang, J., Ding, T., Liu, T., Tsang, H.K., Goda, K., Cheng, Z.: High-Q silicon microring resonator with ultrathin sub-wavelength thicknesses for sensitive gas sensing. Appl. Phys. Rev. **11**(2), 021417 (2024)
31. Wang, X., Yuan, T., Wu, J., Chen, Y., Chen, X.: Enhanced temperature sensing by multi-mode coupling in an on-chip microcavity system. Laser Photonics Rev. **18**(4), 2300760 (2024)
32. Chen, W., Kaya Özdemir, Ş, Zhao, G., Wiersig, J., Yang, L.: Exceptional points enhance sensing in an optical microcavity. Nature **548**(7666), 192–196 (2017)
33. Shao, L., Jiang, X.F., Yu, X.C., Li, B.B., Clements, W.R., Vollmer, F., Wang, W., Xiao, Y.F., Gong, Q.: Detection of single nanoparticles and lentiviruses using microcavity resonance broadening. Adv. Mater. **25**(39), 5616–5620 (2013)
34. Xu, L., Jiang, X., Zhao, G., Ma, D., Tao, H., Liu, Z., Omenetto, F.G., Yang, L.: High-Q silk fibroin whispering gallery microresonator. Opt. Express **24**(18), 20825 (2016)

35. Li, J., Tang, M., Duan, J., Xu, X., Xu, K., Ma, L., Wang, J.: Exceptional points in a spiral ring cavity for enhanced biosensing. J. Lightwave Technol. **41**(9), 2870–2878 (2023)
36. Yin, Y., Pang, J.B., Wang, J.W., Lu, X.Y., Hao, Q., Naz, E.S.G., Zhou, X.X., Ma, L.B., Schmidt, O.G.: Graphene-activated optoplasmonic nanomembrane cavities for photodegradation detection. ACS Appl. Mater. Interfaces **11**(17), 15891–15897 (2019)
37. Zhang, J., Zhong, J., Fang, Y.F., Wang, J., Huang, G.S., Cui, X.G., Mei, Y.F.: Roll up polymer/oxide/polymer nanomembranes as a hybrid optical microcavity for humidity sensing. Nanoscale **6**(22), 13646–13650 (2014)
38. Ma, L.B., Li, S.L., Quiñones, V.A.B., Yang, L.C., Xi, W., Jorgensen, M., Baunack, S., Mei, Y.F., Kiravittaya, S., Schmidt, O.G.: Dynamic molecular processes detected by microtubular opto-chemical sensors self-assembled from prestrained nanomembranes. Adv. Mater. **25**(16), 2357–2361 (2013)
39. Wang, J.W., Karnaushenko, D., Medina-Sánchez, M., Yin, Y., Ma, L.B., Schmidt, O.G.: Three-dimensional microtubular devices for lab-on-a-chip sensing applications. ACS Sens. **4**(6), 1476–1496 (2019)
40. Zhong, J., Wang, J., Huang, G., Yuan, G., Mei, Y.: Effect of physisorption and chemisorption of water on resonant modes of rolled-up tubular microcavities. Nanoscale Res. Lett. **8**(1), 531 (2013)
41. Yin, Y., Wang, J.W., Wang, X.X., Li, S.L., Jorgensen, M.R., Ren, J.F., Meng, S., Ma, L.B., Schmidt, O.G.: Water nanostructure formation on oxide probed *in situ* by optical resonances. Sci. Adv. **5**(10), eaax6973 (2019)
42. Saggau, C.N., Gabler, F., Karnaushenko, D.D., Karnaushenko, D., Ma, L., Schmidt, O.G.: Wafer-scale high-quality microtubular devices fabricated via dry-etching for optical and microelectronic applications. Adv. Mater. **32**(37), 2003252 (2020)
43. Yin, Y., Li, S., Bottner, S., Yuan, F., Giudicatti, S., SaeiGhareh Naz, E., Ma, L., Schmidt, O.G.: Localized surface plasmons selectively coupled to resonant light in tubular microcavities. Phys. Rev. Lett. **116**(25), 253904 (2016)
44. Wang, J., Yin, Y., Hao, Q., Huang, S., Saei Ghareh Naz, E., Schmidt, O.G., Ma, L.: External strain enabled post-modification of nanomembrane-based optical microtube cavities. ACS Photonics **5**(5), 2060–2067 (2018)
45. Yin, Y., Wang, J., Lu, X., Hao, Q., Saei Ghareh Naz, E., Cheng, C., Ma, L., Schmidt, O.G.: *In situ* generation of plasmonic nanoparticles for manipulating photon–plasmon coupling in microtube cavities. ACS Nano **12**(4), 3726–3732 (2018)
46. Wang, J., Tang, M., Yang, Y.D., Yin, Y., Chen, Y., Saggau, C.N., Zhu, M., Yuan, X., Karnaushenko, D., Huang, Y.Z., Ma, L., Schmidt, O.G.: Steering directional light emission and mode chirality through postshaping of cavity geometry. Laser Photonics Rev. **14**(10), 2000118 (2020)
47. Strelow, C., Rehberg, H., Schultz, C.M., Welsch, H., Heyn, C., Heitmann, D., Kipp, T.: Optical microcavities formed by semiconductor microtubes using a bottlelike geometry. Phys. Rev. Lett. **101**(12), 127403 (2008)
48. Strelow, C., Schultz, C.M., Rehberg, H., Sauer, M., Welsch, H., Stemmann, A., Heyn, C., Heitmann, D., Kipp, T.: Light confinement and mode splitting in rolled-up semiconductor microtube bottle resonators. Phys. Rev. B **85**(15), 155329 (2012)
49. Wang, J., Zhan, T.R., Huang, G.S., Chu, P.K., Mei, Y.F.: Optical microcavities with tubular geometry: properties and applications. Laser Photonics Rev. **8**(4), 521–547 (2014)
50. Wang, J., Yin, Y., Yang, Y.D., Hao, Q., Tang, M., Wang, X., Saggau, C.N., Karnaushenko, D., Yan, X., Huang, Y.Z., Ma, L., Schmidt, O.G.: Deterministic yet flexible directional light emission from spiral nanomembrane cavities. ACS Photonics **6**(10), 2537–2544 (2019)
51. Johnson, S.G., Ibanescu, M., Skorobogatiy, M.A., Weisberg, O., Joannopoulos, J.D., Fink, Y.: Perturbation theory for maxwell's equations with shifting material boundaries. Phys. Rev. E **65**(6), 066611 (2002)
52. Mo, C.M., Zhang, L., Xie, C., Wang, T.: Luminescence of nanometer-sized amorphous silicon nitride solids. J. Appl. Phys. **73**(10), 5185–5188 (1993)
53. Vlasukova, L., Parkhomenko, I., Komarov, F., Akilbekov, A., Murzalinov, D., Mudryi, A., Ryabikin, Y., Romanov, I., Giniyatova, S., Dauletbekova, A.: Luminescence of silicon nitride films implanted with nitrogen ions. Mater. Res. Express **5**(9), 096414 (2018)
54. Ward, C.A., Findlay, R.D., Rizk, M.: Statistical rate theory of interfacial transport. I. Theoretical development. J. Chem. Phys. **76**(11), 5599–5605 (1982)
55. Elliott, J.A.W., Ward, C.A.: Temperature programmed desorption: a statistical rate theory approach. J. Chem. Phys. **106**(13), 5677–5684 (1997)
56. Plazinski, W., Rudzinski, W., Plazinska, A.: Theoretical models of sorption kinetics including a surface reaction mechanism: a review. Adv. Colloid Interface Sci. **152**(1–2), 2–13 (2009)
57. Rudzinski, W., Plazinski, W.: On the applicability of the pseudo-second order equation to represent the kinetics of adsorption at solid/solution interfaces: a theoretical analysis based on the statistical rate theory. Adsorption **15**(2), 181–192 (2009)
58. Ofomaja, A.E., Naidoo, E.B., Modise, S.J.: Dynamic studies and pseudo-second order modeling of copper(II) biosorption onto pine cone powder. Desalination **251**(1–3), 112–122 (2010)
59. Bashiri, H.: Desorption kinetics at the solid/solution interface: a theoretical description by statistical rate theory for close-to-equilibrium systems. J. Phys. Chem. C **115**(13), 5732–5739 (2011)

Mingquan Deng obtained his B.S. degree in Optoelectronic Information Science and Engineering from the School of Physics at Changchun University of Science and Technology, Changchun, China, in 2023. He is currently pursuing his master degree at School of Integrated Circuits, Harbin Institute of Technology (Shenzhen), Shenzhen, China. His research primarily focuses on whispering-gallery-mode optical microcavity molecular sensing.

Xiujie Dou is currently a postdoctoral researcher in School of Integrated Circuits, Harbin Institute of Technology (Shenzhen), Shenzhen, China. She obtained her Ph.D. degree in Physics from Delft University of Technology, the Netherlands, in 2024. Her specific areas of interest include micro-nano optical field modulation, optical scatterometry, optical microcavities and molecular sensing.

Xiaoyu Wang is an associate professor in the School of Physics and Optoelectronic Engineering, Hainan University, Haikou, China. She received her Ph.D. in Physics at the Technische Universität Dresden, Germany, in 2022. Her research focuses on micro/nanophotonics and its optoelectronic applications, including optical microcavities, dynamic light modulation devices, and spectrally selective absorption films.

Yin Yin is a professor in the School of Materials Science and Engineering in Jiangsu University, China. He obtained his Ph.D. degree in Electrical Engineering and Information Technology from Chemnitz University of Technology, Germany, in 2018. His current research interests include cavity photonics, topological photonics, plasmonics, and light-matter interactions.

Xun Guan has been an Assistant Professor in the Tsinghua Shenzhen International Graduate School, Tsinghua University, Shenzhen, China, since 2022. He got his Ph.D. degree in Information Engineering from The Chinese University of Hong Kong, China, in 2016, and worked in the Centre for Optics, Photonics and Laser, Universite Laval, Canada, as a postdoctoral researcher and then a research scientist, from 2017 to 2022. His main research area spans extensively across optical sensing and optical communication, while actively incorporating of integrated photonics and deep learning.

Libo Ma is a research group leader in the Institute of Integrative Nanosciences at Leibniz IFW Dresden, Germany. He received his B.S. degree in Physics from Shandong Normal University, China, in 2001. He obtained his Ph.D. degree from the Institute of Physics, Chinese Academy of Sciences, China, in 2007. His current research interests include cavity photonics, plasmonics, light-matter interactions, on-chip photonic integration, and topological photonics.

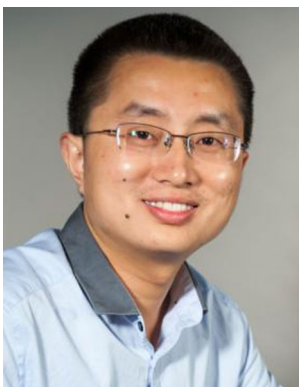

Xing Ma is a professor in the School of Integrated Circuits, Harbin Institute of Technology (Shenzhen), Shenzhen, China. He obtained his Ph.D. degree from Materials Science and Engineering School at Nanyang Technological University, Singapore, in 2013. He was awarded the Alexander von Humboldt fellowship for his postdoc research at the Max-Planck Institute for Intelligent Systems at Stuttgart Germany. His research interest focuses on smart biomaterials for micro/nano-robots or motors and biosensing devices. He has published more than 140 papers, with citations higher than 14,000 and H-index of 68.

Jiawei Wang is a professor in the School of Integrated Circuits, Harbin Institute of Technology (Shenzhen), Shenzhen, China. He received his Ph.D. degree in Electronic and Computer Engineering at the Hong Kong University of Science and Technology, China, in 2016. He worked as a postdoctoral researcher at Leibniz IFW Dresden and a research associate at the Chemnitz University of Technology from 2016 to 2020. His research group explores integrated photonics, especially cavity photonics, and their applications in healthcare and environmental sensing.